DESIGN AND FABRICATION OF SHAPE MORPHING MAGNETO-IMPEDANCE MAGNETIC SENSOR

Van Thin Pham[1], Hai Ninh Dang[1], Quang Dat Tran[1], Dinh Vi Le[1], Van Trung Tong[2], Thi Thanh Ngo[3], Thi Ngoc Nguyen[4], Nguyen Thuc Vu[5], Anh Tam Ho[5], Thi Huong Giang Do[3,5], Van Tuan Nguyen[1,*]

[1]*Faculty of Physics and Chemical Engineering, Le Quy Don Technical University*

[2]*Electronic Factory Z181*

[3]*Faculty of Physics Engineering and Nanotechnology, VNU University of Engineering and Technology, Vietnam National University, Hanoi*

[4]*Department of Advanced Materials Science and Nanotechnology, University of Science and Technology of Hanoi, Vietnam Academy of Science and Technology*

[5]*VNU Key Laboratory for Micro-Nano Technology, VNU University of Engineering and Technology, Vietnam National University, Hanoi*

Abstract

The magnetoimpedance (MI) effect is characterized by the alteration in the impedance of soft magnetic materials when subjected to a magnetic field while a high-frequency alternating current flows through them. In this study, we engineered two distinct sensor architectures utilizing amorphous FeCSi magnetic ribbon: a single-bar structure with the dimension of 10 mm × 90 µm × 20 µm and a meander structure consisting of 13 parallel single bars. These structures were miniaturized through advanced techniques combining laser engraving and chemical etching. The magnetic analysis reveals that the meander structure exhibits a pronounced dependency on the angle θ between the magnetic field and the sensor orientation, enhancing its soft magnetic properties by up to fivefold compared to the single-bar design. This enhancement might be attributed to a reduction in the demagnetization effect and shape anisotropy energy within the meander sensor. Furthermore, the analysis of the MI effect indicates that the resonance frequency remains unaffected by external magnetic fields for both sensor types. Notably, the meander sensor demonstrates exceptional MI ratio values exceeding 82%, representing a remarkable 24-fold increase over the 3.5% observed in the single-bar sensor. Additionally, the isotropy - quantified as the MI ratio's dependence on angle θ, and magnetic field sensitivity are significantly improved in the meander configuration. These advancements in soft magnetic and physical properties are correlated to the domain structure of the sensor, particularly its transverse magnetic permeability, as evidenced by micromagnetic simulations conducted using Mumax[3]. With its superior MI ratio, isotropy, and heightened magnetic field sensitivity, the meander-type magnetic field sensor presents substantial potential for applications across diverse fields, ranging from biological systems to specialized practical missions.

Keywords: *Magnetoimpedance sensor; magnetic sensors; magnetic energies; isotropy.*

[*] Corresponding author email: tuannv@lqdtu.edu.vn

DOI: 10.56651/lqdtu.jst.v2.n02.875.pce

1. Introduction

The magnetoimpedance (MI) effect is characterized by significant variations in the impedance of metallic magnetic conductors when subjected to a DC magnetic field [1, 2]. Impedance is typically measured using a four-point technique, at which an AC current flows through the sample, and the voltage is measured to determine both real and imaginary components that contribute to MI. This phenomenon is rooted in the classical electromagnetic skin effect, for which high-frequency currents are confined to a thin surface layer of the conductor [3, 4]. The penetration depth is inversely related to the material's conductivity, permeability, and the frequency of the AC current, which induce higher conductivity and permeability, resulting in reduced skin depth.

Although MI was known earlier, its observation in various magnetic materials with considerable electrical conductivity only occurred in the 1990s. Applying a DC magnetic field alters the magnetic permeability of these materials, consequently affecting the skin depth and impedance. To effectively observe MI, materials with high permeability that a DC field can modify are essential. Therefore, MI is most pronounced in ultrasoft magnetic materials with high electrical conductivity, by which their thickness aligns with changes in skin depth induced by the DC field [5-7]. MI is especially prominent in soft amorphous materials such as ribbons [8-12] and wires [13, 14], exhibiting softness and relatively high conductivity. The frequency range for observing MI typical spans from 100 kHz to 10 MHz, often increasing with frequency [15]. While less soft materials like thin films and multilayers typically demonstrate MI, their effectiveness varies. Moreover, the relationship between MI and ferromagnetic resonance has been explored extensively, at which resonance phenomena generally manifest in the GHz range, with natural ferromagnetic resonance detected between 2 and 12 GHz for amorphous microwires, depending on their magnetostriction constant. MI elements are integral to developing highly sensitive magnetic field sensors [16]. These sensors, particularly those made from amorphous wires, are currently utilized in mobile phone compasses and are under investigation for potential medical applications and nondestructive testing methods. Ongoing research focuses on enhancing MI elements by optimizing materials, controlling anisotropy, refining sensor structures, and developing theoretical models to improve sensitivity, especially in wires and ribbons [10, 11, 13, 14, 17-19].

The miniaturization of electronic devices and advancements in rapid signal processing have necessitated the reduction in size of MI elements. Thin film and/or ribbon configurations present a promising avenue for achieving this miniaturization, as they can be integrated with electronic devices. However, this size reduction may compromise

the sensitivity of MI sensors due to the emergence of demagnetizing fields [20, 21]. Although various attempts have been made to dedicate the intrinsic properties of the MI, a more precise understanding of extrinsic properties such as shape anisotropy, demagnetizing effects is essential for optimizing sensor design sensitivity [22, 23]. In this study, the MI elements were micropatterned into desired shapes of single bar and meander forms with a sided-width of 100 µm, which is known to be close to the optimized value of 60 µm [24]. These sensor configurations allow to evaluate the influence of shape anisotropy and the demagnetizing field to the overall MI effect. The investigations were conducted for global magnetic characterization of vibrating sample magnetometer (VSM), impedance measurements, and domain observations through micromagnetic simulation for each element as changes in domain structures provide critical insights into sensor behavior. Additionally, detailed analysis of shape anisotropy and demagnetizing field was correlated with the magnetic properties that contributed to the MI. Our findings highlight how the shape anisotropy and demagnetizing field in various forms affect the MI effect and propose a method to enhance sensitivity in MI sensors.

2. Materials and methods

2.1. Sensor fabrication and experimental characterizations

A series of MI elements were microstructured using a combination of wet chemical and laser etching techniques on an amorphous commercial ribbon with a nominal composition of $Fe_{91}Si_4C_5$, possessing an average thickness of 20 µm. The fabrication process comprises five key stages following protocols established in previous studies, as described elsewhere [24, 25]. Magnetic characterization of the MI elements was conducted using a global approach of vibrating sample magnetometer (VSM, Lakeshore 7400 series) with a maximum applied magnetic field of 1.8 T. The fabricated sensor was positioned within a sample holder for MI measurement, as depicted in Fig. 1. The experimental setup included a network analyzer of Protek A333, which supplied alternating current (AC) at various frequencies to the developed sensors. The sensors were strategically placed between two permanent magnets, allowing for magnetic field adjustments up to 400 Oe by varying the distance between the magnets. This comprehensive system facilitates the manipulation of multiple parameters, including the DC-applied field and frequency, to elucidate the operational characteristics of the fabricated MI elements.

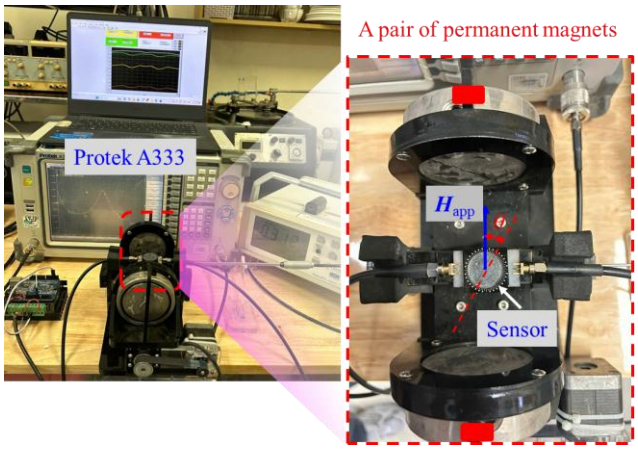

Fig. 1. The characterization setup for MI measurement showing the vector network analyzer for impedance recording, movable pair of permanent magnets for controlling the applied magnetic field, the sample holder, and the schematic for angle between the applied magnetic field and the longitudinal direction of the developed sensors.

2.2. Micromagnetic simulation

Micromagnetic simulation of the meander-structured sensor was conducted utilizing the open-source software MuMax^3, developed in Go and incorporating CUDA for enhanced performance on graphics processing units (GPUs) [26, 27]. GPUs significantly accelerates computational speed, enhancing several orders of magnitude compared to traditional central processing unit (CPU) operations. In this study, the simulation models were discretized into cubic cells with dimensions of approximately 2.5 nm, notably smaller than the exchange length characteristic of the soft magnetic material FeCSi [28]. To replicate the grain structure, grain-like regions were generated within the simulated elements using Voronoi mosaics. Additionally, variations in magnetic grain parameters were introduced, with a fluctuation of up to 15% in both magnetization and exchange constant, reflecting the actual diversity in grain height and properties observed on the sensor surface. The boundaries between grains were defined as magnetic, reflecting the scale exchange term within the simulation framework. MuMax^3 employs the Landau–Lifshitz–Gilbert equation at each node to model magnetization dynamics, assuming that each magnetic moment is positioned at the center of its respective cell and that exchange interactions occur at the discrete surfaces of these cells.

3. Results and discussion

Figure 2 presents top-view photographs of the fabricated sensors, displaying both single-bar and meander structures (Fig. 2a1, 2b1). The images reveal that the edges of the sensor structures are flat and well-defined, confirming the successful fabrication of

the sensors. Fig. 2a2 and 2b2 further illustrate that the edges are smooth and straight, with an edge width of approximately 90 µm. This measurement indicates a slight reduction of about 10% compared to the design specification of 100 µm, attributed to the isotropic nature of the wet chemical etching process employed during the five-step fabrication as indicated in the Experimental section. Fig. 2a3 and 2b3 define the angle θ of the external magnetic field with respect to the horizontal direction aligned with the longitudinal edge of the sensor.

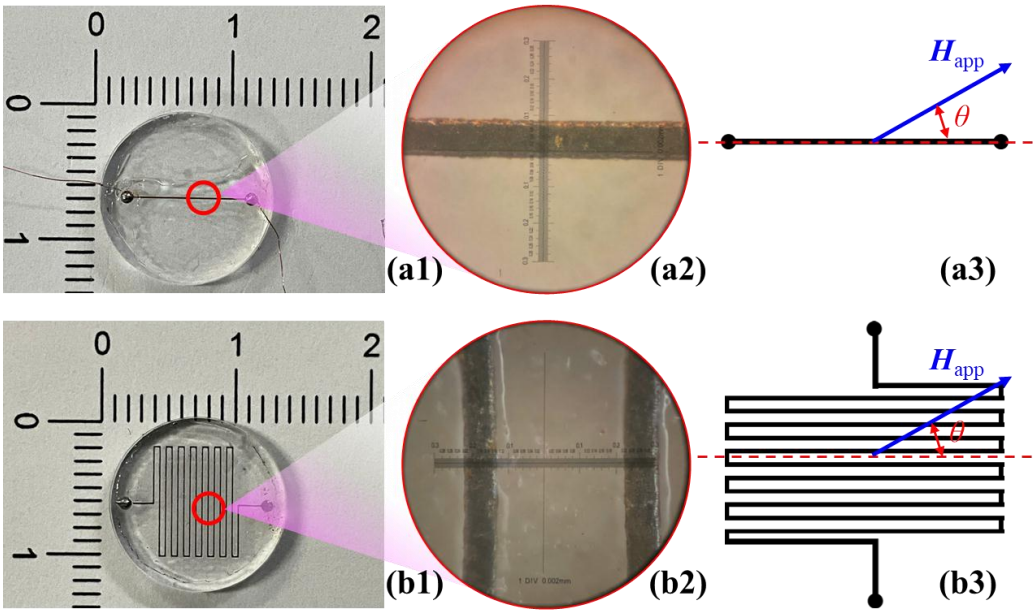

Fig. 2. The photographs, optical images with high magnification of the developed sensors in the forms of single bar (a1-a2) and meander (b1-b2); and the illustrations for the angle θ between the applied magnetic field and the horizontal line of the developed sensors (a3, b3).

Figure 3a and 3b display the normalized hysteresis $M(H)$ loops for the fabricated sensor structures, characterized within a range of -0.5 T to 0.5 T. The results indicate that single-bar and meander sensors exhibit coercivity values below 0.5 Oe (or 50 µT), demonstrating that the samples retain the soft magnetic properties characteristic of the original amorphous FeCSi material. This finding is crucial, as it confirms that the fabrication processes of combining laser engraving and wet chemical etching do not induce the phase of the sensor material. The $M(H)$ curve analysis reveals that as angle θ increases, magnetization becomes magnetically hard. Specifically, at $\theta = 0°$, both sensor structures achieve saturation at an external magnetic field of approximately 0.2 T. In contrast, reaching saturation at $\theta = 45°$ requires an external magnetic field nearly double that at $\theta = 0°$, approximately 0.4 T. Additionally, for angles $\theta \leq 30°$, the slope of the $M(H)$ loop for the meander structure is generally higher towards the vertical axis

compared to that of the single-bar structure. This distinction in the slopes of $M(H)$ loops becomes more pronounced with increasing θ for the meander structure, while it remains less evident for the single-bar structure.

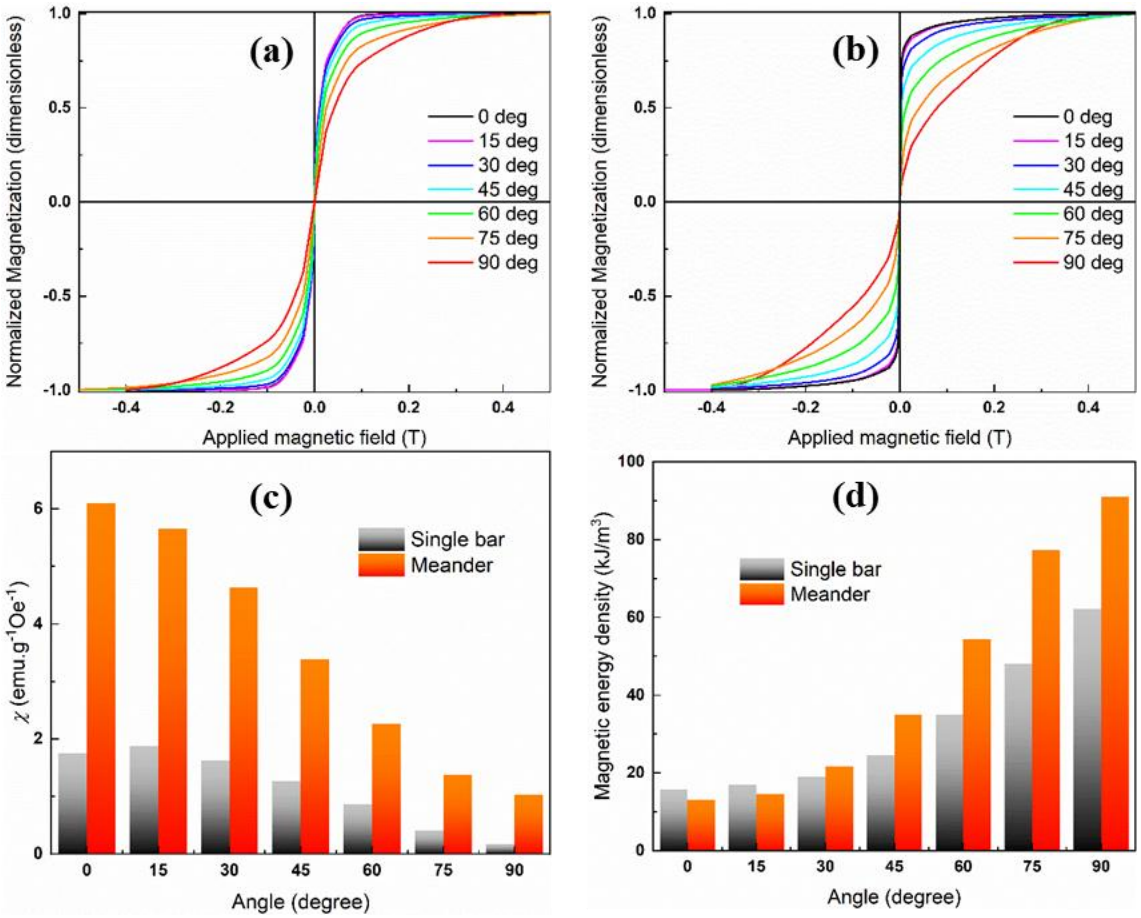

Fig. 3. The major normalized hysteresis M(H) loops, which is not corrected for demagnetizing field, for single bar (a) and meander (b) sensors; the derived magnetic susceptibilities (c) from the normalized M(H) loops from (a) and (b); and the estimated magnetic energy anisotropy and/or magnetic energy density (d) of the developed sensors.

A key parameter for evaluating soft magnetic properties is magnetic susceptibility (χ), which is typically calculated as the first derivative of magnetization with respect to applied external magnetic field at the coercive force value. This study derived the χ from the major $M(H)$ loops. Figure 3c illustrates how the χ varies with angle θ for the fabricated sensor samples. Notably, at angles $\theta \leq 45°$, the χ of the meander structure is approximately three times greater than that of the single-bar structure. This disparity increases to about fivefold when $\theta = 90°$. The analysis indicates a significant enhancement in soft magnetic properties for the meander structure, improving from

three to five times compared to its conventional single-bar counterpart.

To assess the variation in the χ at different angles θ, this study examines the shape magnetic anisotropy energy, or magnetic energy density, calculated using the following expression as follows: $\int_0^{M_s} HdM$, where M_s is the saturation magnetization. Figure 3d illustrates the dependence of this energy on angle θ. For the single-bar structure, the magnetic energy density remains relatively constant at approximately 20 kJ/m³ for angles $\theta \leq 45°$. However, at angles $\theta = 75°$ and 90°, the shape magnetic anisotropy energy increases sharply by factors of about two and three, respectively. A similar tendency is observed in the meander structure. Notably comparing the anisotropy energy at $\theta = 90°$ to that at $\theta = 0°$, a substantial increase of approximately nine times is recorded for the meander structure. This suggests a degradation in the soft magnetic quality of the meander structure at larger angles θ. The pronounced difference in shape anisotropy energy relative to the angle between the sensor and the applied external magnetic field is believed to stem from variations in demagnetization field energy. Specifically, in the single-bar structure, as the direction of the magnetic field shifts from 0° to 90°, the demagnetization field coefficient escalates significantly from 0.00176 to 0.21219 with a factor of 120 [29, 30]. In contrast, for the meander structure, characterized by 13 long edges and shorter edges continuously coupled to them, the demagnetization field coefficient is markedly reduced compared to that of the single-bar structure.

Figure 4a and 4b depict the relationship between the MI effect and frequency, measured under a direct current (DC) external magnetic field ranging from 0 to 400 Oe at an angle $\theta = 0°$. Initially, the impedance signal exhibits a sharp decline within the frequency range of 0-1 GHz for the single-bar sensor and 0-0.5 GHz for the meander sensor. Subsequently, the impedance signal rises sharply to reach a maximum value at resonant frequencies of 1.8 GHz for the single-bar structure and 1.1 GHz for the meander structure. Beyond this frequency threshold, a rapid decrease in impedance is observed. Importantly, throughout this study, resonant frequency values remain consistent despite variations in angle θ, agreeing well with those reported for other structures such as 2D spiral square amorphous wires or FeCuNbSiB monolayer/multilayer thin films [7, 16].

Other studies on high-frequency MI effects have indicated that multiple peaks may emerge within frequency-dependent MI curves, suggesting that resonance can occur at various frequencies [31-33]. The interplay between ferromagnetic resonance modes and spin wave modes inspired by the gyromagnetic effect is the main

contribution to the multiple peak presence. However, this study focuses on frequencies below 2 GHz to elucidate the mechanisms underlying the MI effect associated with magnetization processes. Literature suggests that distinct bands of the MI effect can be delineated based on AC frequencies applied through the sensing samples [34]. The MI effect observed with frequency from 1 to 2 GHz are primarily related to modifications in transverse permeability, at which the skin effect is present [31, 35, 36].

To investigate the impedance effect illustrated in Fig. 2, the following formula was employed to calculate the MI ratio of the fabricated sensors, enabling an evaluation of the relative impedance changes between the samples:

$$MI\left(\%\right)=\frac{Z\left(H\right)-Z\left(H=0\right)}{Z\left(H=0\right)}\times 100$$

where $Z(H)$ represents the sensor's impedance under a specific applied external magnetic field, and $Z(H = 0)$ denotes the impedance when no external magnetic field is applied.

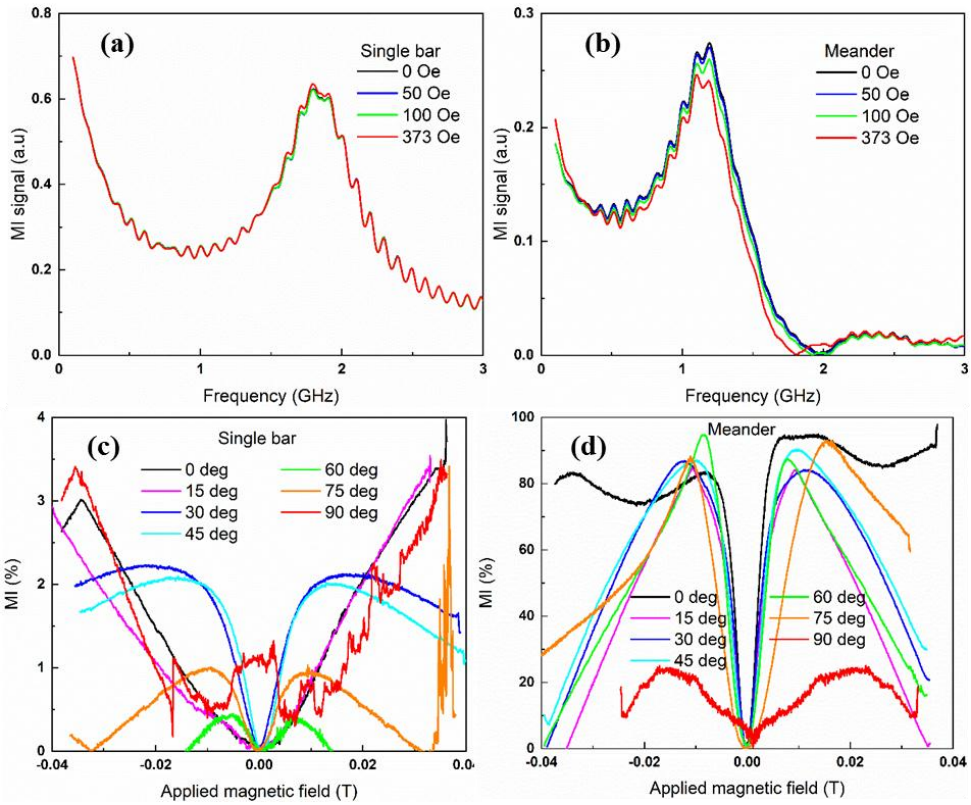

Fig. 4. The dependence of magnetoimpendance signal on the exciting frequency for the single bar (a) and meander (b) sensors; and the change in MI ratio as a function of the applied magnetic field in the range of - 0.04 T to 0.04 T for the set of developed sensors (c-d).

Figure 4c and 4d present a comparative analysis of the MI ratios for the fabricated single-bar and meander sensors. MI measurements were conducted under a magnetic field of up to 400 Oe at varying angles θ. For the single-bar structure, at angles $\theta \leq 15°$, the MI curve exhibits a V-shaped profile, indicating that the MI ratio is directly proportional to the applied magnetic field. As the angle θ increases, this response transitions to an inverted W-shaped curve, with a linear response range for the MI curve confined to approximately ±100 Oe. Notably, across all tested conditions, the MI ratio for the single-bar structure remains limited to around 3.5%. This finding indicates the minimal MI effect in the single-bar configuration. In contrast, the meander structure demonstrates a markedly improved MI response. Specifically, for angles ranging from 0° to 75°, the MI ratio consistently exceeds 82%. However, this ratio diminishes significantly at θ = 90°. The meander structure maintains a linear operational range comparable to the single-bar structure, approximately ±100 Oe. Despite comprising 13 bars in length compared to a single bar, the meander configuration enhances the MI ratio by nearly 24 times. This observation highlights that the MI ratio in MI effect is influenced not only by the number of sensing elements but also by the soft magnetic properties of the fabricated material, i. e., the reduction in demagnetization field and variations in shape anisotropy energy evidenced previously.

With the aim to further elucidate the distinctive characteristics of the two sensor types based on their MI response, i.e., the operating range where changes in the MI effect are most pronounced and the sensitivity of each sensor to magnetic field variations, this study calculated the magnetic sensitivity by taking the first derivative of the MI ratio with respect to the applied magnetic field ($\delta MI / \delta H$). Figure 5a and 5b illustrate the magnetic sensitivity of both the single-bar and meander sensors, emphasizing their optimal operating conditions. For both sensor configurations, magnetic sensitivity peaks at the magnetic field point, by which the MI curve exhibits its steepest slope. The maximum magnetic sensitivity $\left(\delta MI / \delta H\right)_{\max}$ for the single-bar sensor is relatively low, approximately 0.037 %/Oe, occurring at an angle θ = 45°. Deviations from this angle result in a decline in the values of $\left(\delta MI / \delta H\right)_{\max}$. In contrast, the meander sensor achieves $\left(\delta MI / \delta H\right)_{\max}$ nearly 80 times greater than the single-bar sensor, with increasing angles θ corresponding to shifts toward higher magnetic fields. This characteristic is particularly significant for potential applications of the meander sensor in biomedical contexts, such as detecting magnetically labeled biological elements.

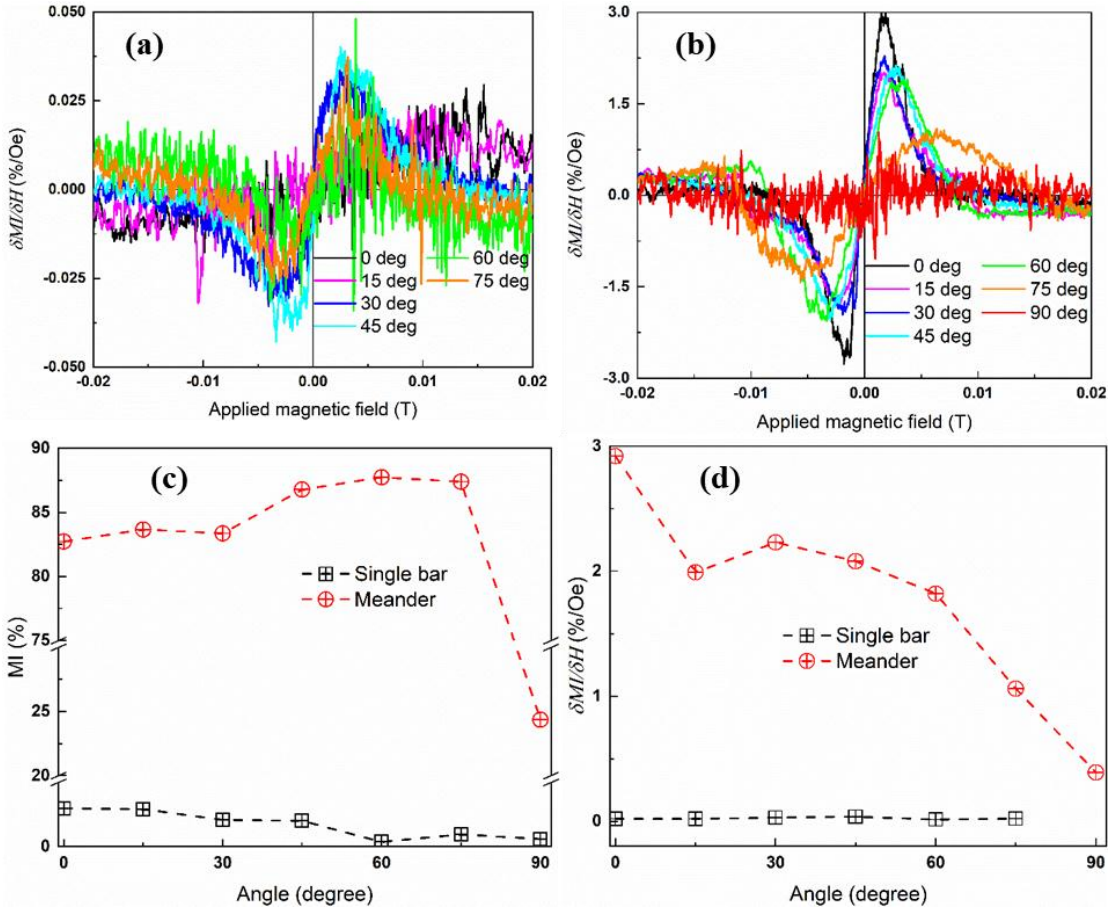

Fig. 4. The derived sensitivities of single bar (a) and meander (b) sensors by taking the first derivative of MI ratio with respect to the applied magnetic field; and the dependences of MI ratio (c) and the derived sensitivity (d) as functions of applied magnetic field for the developed sensors.

The advantages of the meander sensor over the single-bar design were further conducted regarding the dependence of the MI ratio on angle θ (as depicted in Fig. 5c and 5d). When varying θ between 0° and 75°, the MI ratio for the meander sensor fluctuates only about 6%, rising from 82.5% at 0° to approximately 87.5% at 75°. In contrast, this fluctuation reaches nearly 50% for the single-bar structure. Similar trends are observed when evaluating other parameters of the fabricated sensors. It is evident that metrics such as magnetic sensitivity, MI ratio, and isotropy, expressed through their dependences on angle θ, are significantly greater for the meander sensor than the single-bar structure. This enhanced performance positions the meander structure as advantageous for specific applications requiring high sensitivity and isotropy. The superiority of the meander sensor is believed to be closely linked to its domain structure under varying magnetic field conditions, which serves to minimize different forms of

magnetic energy [31, 35, 36]. To further clarify these findings, micromagnetic simulations were conducted using Mumax[3], focusing on the meander structure under varying θ.

Figure 6 demonstrates a strong correlation between the normalized hysteresis curves $M(H)$ obtained experimentally and those derived from micromagnetic simulation of the meander structure at different angles θ. This alignment confirms the validity of Mumax[3] simulation employed in this study, reinforcing our understanding of how domain properties differences impact the sensor characteristics.

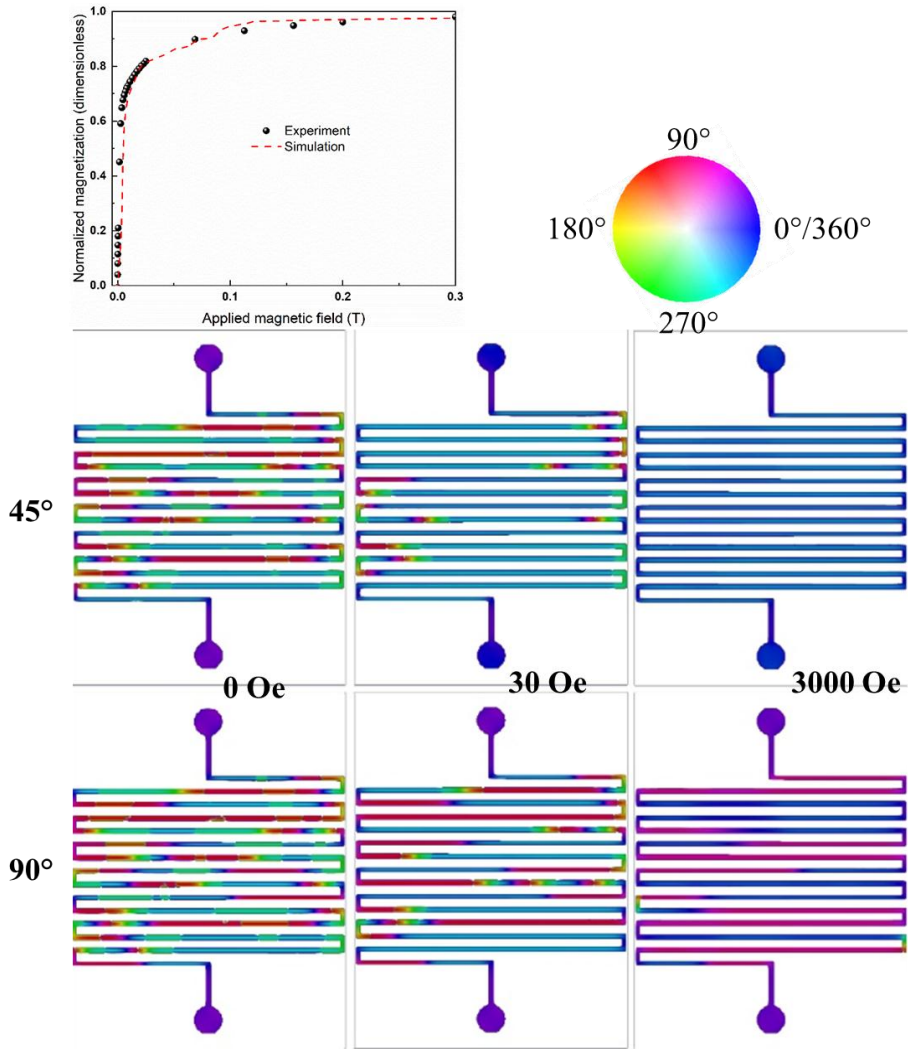

Fig. 5. The normalized M (H) as a function of applied magnetic field for both cases of experiment and simulation (θ = 30°) demonstrates the validity of Mumax[3] simulation, and the evolution of domain structure at three distinct values of applied magnetic field with θ = 45° and 90°.

Figure 6 illustrates the changes in domain structure as a function of the applied external magnetic field for angles θ = 45° and θ = 90°. The angle θ = 45° was selected for analysis as it represents the midpoint within the range of isotropic MI signals corresponding to angles of 0°, 15°, 30°, 60°, and 75°. Conversely, θ = 90° was chosen due to its distinctly different MI signal compared to the other angles. Without external magnetic field, both configurations exhibit multi-domain structures with minimal differences between them. When the magnetic field is increased to approximately 30 Oe, the point at which the MI signal curve is steepest, the θ = 90° case reveals multi-domain structures throughout nearly all sensor branches, characterized by adjacent domains oriented at 180° to each other. In contrast, at θ = 45°, the multi-domain nature is significantly diminished, leading to the emergence of single-domain structures. As the magnetic field is further increased to a maximum value of 0.3 T, complete saturation occurs in all sensor branches at θ = 45°, resulting in a uniform single-domain structure across the sensor. While some branches exhibit a single-domain structure at this high magnetic field, others retain a multi-domain configuration. However, the domain sizes are substantially larger than those observed without an applied magnetic field. This behavior can be attributed to competition among various forms of magnetic energy, i. e., Zeeman energy, shape anisotropy, and demagnetization field, under the influence of an external magnetic field aligned with the sensor's hard magnetization direction. Consequently, energy minimization favor the formation of diverse domain structures. Thus, it can be concluded that the sensor's domain structure is influenced by both its orientation relative to the magnetic field and the magnitude of the applied external magnetic field.

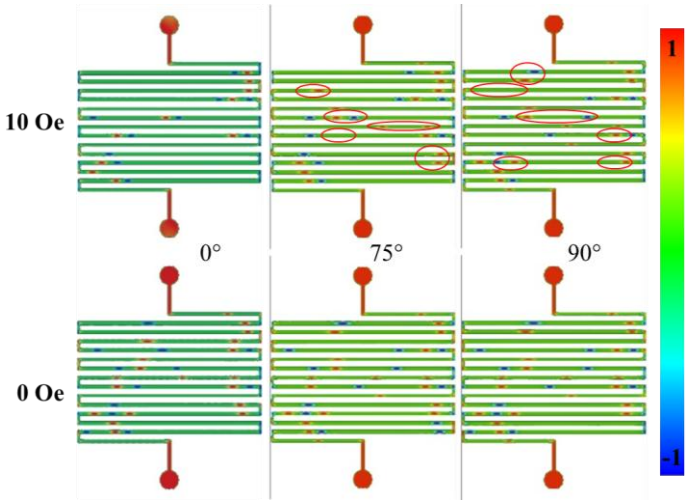

Fig. 7. The evolution of transverse magnetization components in the meander sensors with various values of θ, under distinct applied magnetic field.

The MI effect is significantly influenced by changes in the domain structure, particularly the transverse magnetic moment component related to transverse magnetic permeability [1, 35, 37]. The simulation results for the meander sensor structure will be further explored following this context. Figure 7 illustrates the variation in the transverse magnetic moment component, which is perpendicular to the current flowing through the sample and represents the transverse magnetic permeability. Notably, a magnetic field value of 10 Oe yields the largest $(\delta MI / \delta H)_{\max}$. For angles θ ranging from 0° to 60°, the transverse magnetic moment component remains relatively stable across different external magnetic fields, and thus is not depicted in the shown figures. Red ellipses highlight the differences in the transverse magnetic magnetic component for three cases. The contribution of the transverse magnetic moment component increases significantly at θ = 90°, agreeing with experimental observations that show a marked decrease in MI ratio at this angle compared to others. Even when the magnetic field is turned off, differences in the transverse magnetic moment component persist across varying θ cases, contributing to the MI effect. This analysis indicates that both the transverse magnetic permeability and domain formation under different external magnetic fields, along with the orientation angle between the sensor and the external magnetic field, play crucial roles in controlling the magnetization process and influencing the MI effect.

4. Conclusion

Two sensor structures of a single-bar and a meander configuration were fabricated using advanced laser engraving and wet chemical etching techniques with miniaturized FeCSi amorphous magnetic ribbon. Magnetic property analyses indicated that the meander structure exhibits enhanced soft magnetic properties, achieving up to five times the performance of the single-bar design. This improvement is due to 13 additional magnetic sensing elements, and reduction in demagnetization field and shape magnetic anisotropy energy. Consequently, the meander structure's MI ratio exceeds 82%, a remarkable 24-fold increase over the single-bar sensor's 3.5%. It also shows enhanced isotropy, with an MI ratio variation of no more than 6% across angles from -75° to 75°, and a significant magnetic sensitivity of up to 3%/Oe. These advancements are linked to the sensor's magnetic domain structure and confirmed by micromagnetic simulations using MuMax^3. The findings suggest that the meander sensor has substantial potential for applications in various fields, including biomedical contexts. Furthermore, this research establishes a systematic approach for investigating MI sensor systems, facilitating analytical measurements and simulations to clarify the results obtained.

Acknowledgements

This research is funded by Le Quy Don Technical University Research Fund under the grant number 24.1.12.

References

[1] L. V. Panina and K. Mohri, "Magneto-impedance effect in amorphous wires", *Applied Physics Letters*, Vol. 65, pp. 1189-1191, 1994. DOI: 10.1063/1.112104

[2] R. S. Beach and A. E. Berkowitz, "Giant magnetic field dependent impedance of amorphous FeCoSiB wire", *Applied Physics Letters*, Vol. 64, pp. 3652-3654, 1994. DOI: 10.1063/1.111170

[3] C. Kittel, "Theory of the dispersion of magnetic permeability in ferromagnetic materials at microwave frequencies", *Physical Review*, Vol. 70, pp. 281-290, 1946. DOI: 10.1103/PhysRev.70.281

[4] L. Rayleigh, "XXV. Notes on electricity and magnetism. -III. On the behaviour of iron and steel under the operation of feeble magnetic forces, The London, Edinburgh, and Dublin", *Philosophical Magazine and Journal of Science*, Vol. 23, pp. 225-245, 1887. DOI: 10.1080/14786448708628000

[5] D. García, V. Raposo, O. Montero, and J. I. Íñiguez, "Influence of magnetostriction constant on magnetoimpedance-requency dependence", *Sensors and Actuators A: Physical*, Vol. 129, pp. 227-230, 2006. DOI: 10.1016/j.sna.2005.11.046

[6] V. Zhukova, J. M. Blanco, M. Ipatov *et al.*, "Optimization of high frequency magnetoimpedance effect of Fe-rich microwires by stress-annealing", *Intermetallics*, Vol. 94, pp. 92-98, 2018. DOI: 10.1016/j.intermet.2017.12.025

[7] Z. Zhu, M. Peng, Y. Wang, and F. Qin, "Ultra-large giant magnetoimpedance effect by a 2D square spiral amorphous microwire", *Journal of Magnetism and Magnetic Materials* Vol. 550, 2022. DOI: 10.1016/j.jmmm.2022.169090

[8] F. L. A. Machado and S. M. Rezende, "A theoretical model for the giant magnetoimpedance in ribbons of amorphous soft-ferromagnetic alloys", *Journal of Applied Physics*, Vol. 79, pp. 6558-6560, 1996. DOI: 10.1063/1.361945

[9] B. Hernando, M. L. Sánchez, V. M. Prida, M. Tejedor, and M. Vázquez, "Magnetoimpedance effect in amorphous and nanocrystalline ribbons", *Journal of Applied Physics*, Vol. 90, pp. 4783-4790, 2001. DOI: 10.1063/1.1408594

[10] M. Nowicki, P. Gazda, R. Szewczyk *et al.*, "Strain dependence of hysteretic giant magnetoimpedance effect in co-based amorphous ribbon", *Materials*, Vol. 12, 2019. DOI: 10.3390/ma12132110

[11] Z. Yang, A. A. Chlenova, E. V. Golubeva *et al.*, "Magnetoimpedance effect in the ribbon-based patterned soft ferromagnetic meander-shaped elements for sensor application", *Sensors*, Vol. 19, 2019. DOI: 10.3390/s19112468

[12] H. N. Motlagh and G. Rezaei, "Monte Carlo simulation of giant magneto-impedance effect in amorphous ferromagnetic thin films", *Journal of Alloys and Compounds*, Vol. 723, pp. 401-407, 2017. DOI: 10.1016/j.jallcom.2017.06.216

[13] M. Vázquez, "Soft magnetic wires", *Physica B: Condensed Matter*, Vol. 299, pp. 302-313, 2001. DOI: 10.1016/S0921-4526(01)00482-3

[14] M. Vázquez, "Giant magneto-impedance in soft magnetic wires", *Journal of Magnetism and Magnetic Materials*, Vol. 226-230, pp. 693-699, 2001. DOI: 10.1016/S0304-8853(01)00013-0

[15] G. V. Kurlyandskaya, H. Yakabchuk, E. Kisker *et al.*, "Very large magnetoimpedance effect in FeCoNi ferromagnetic tubes with high order magnetic anisotropy", *Journal of Applied Physics*, Vol. 90, pp. 6280-6286, 2001. DOI: 10.1063/1.1418423

[16] M. A. Corrêa, A. D. C. Viegas, R. B. da Silva, A. M. H. de Andrade, and R. L. Sommer, "Magnetoimpedance of single and multilayered FeCuNbSiB films in frequencies up to 1.8GHz", *Journal of Applied Physics*, Vol. 101, 2007, 043905. DOI: 10.1063/1.2512867

[17] J. Nabias, A. Asfour, and J. P. Yonnet, "The impact of bending stress on the performance of giant magneto-impedance (GMI) magnetic sensors", *Sensors*, Vol. 17, 2017. DOI: 10.3390/s17030640

[18] T. Morikawa, Y. Nishibe, H. Yamadera *et al.*, "Giant magneto-impedance effect in layered thin films", *IEEE Transactions on Magnetics*, Vol. 33, pp. 4367-4372, 1997. DOI: 10.1109/20.620448

[19] A. Zhukov, M. Ipatov, P. Corte-León *et al.*, "Giant magnetoimpedance in rapidly quenched materials", *Journal of Alloys and Compounds*, Vol. 814, 2020. DOI: 10.1016/j.jallcom.2019.152225

[20] H. Kikuchi, S. Oe, H. Uetake *et al.*, "Enhancement of Sensitivity on Miniaturized Thin-film Magnetoimpedance with Ellipsoidal Element", *Physics Procedia*, Vol. 75, pp. 1271-1278, 2015. DOI: 10.1016/j.phpro.2015.12.141

[21] A. García-Arribas, E. Fernández, A. V. Svalov *et al.*, "Tailoring the magnetic anisotropy of thin film permalloy microstrips by combined shape and induced anisotropies", *European Physical Journal B*, Vol. 86, 2013, 136. DOI: 10.1140/epjb/e2013-30933-6.

[22] A. García-Arribas, E. Fernández, I. Orue, and J. M. Barandiaran, "Determination of the distribution of transverse magnetic anisotropy in thin films from the second harmonic of Kerr signal", *Applied Physics Letters*, Vol. 103, 2013, 142411. DOI: 10.1063/1.4824647.

[23] H. Kronmüller and B. Gröger, "Domains, domain walls and the coercive field of amorphous ferromagnets", *Journal de Physique France*, Vol. 42, pp. 1285-1292, 1981. DOI: 10.1051/jphys:019810042090128500.

[24] H. A. Tam, N. V. Tuan, N. T. Ngoc *et al.*, "Tuning rotational magnetization for high frequency magnetoimpedance in micro-patterned triangle spiral magnetic systems", *Journal of Science: Advanced Materials and Devices*, Vol. 7, 2022, 100514. DOI: 10.1016/j.jsamd.2022.100514

[25] V. N. Thuc, H. A. Tam, D. T. H. Giang *et al.*, "Hierarchical geometric designs for Fe-based amorphous materials with tunable soft magnetic properties", *Journal of Alloys and Compounds*, Vol. 895, 2022. DOI: 10.1016/j.jallcom.2021.162628

[26] J. J. Joos, P. Bassirian, P. Gypens *et al.*, "Tutorial: Simulating modern magnetic material systems in mumax3", *Journal of Applied Physics*, Vol. 134, 2023, 171101. DOI: 10.1063/5.0160988

[27] A. Vansteenkiste, J. Leliaert, M. Dvornik *et al.*, "The design and verification of MuMax3", *AIP Advances*, Vol. 4, 2014, 107133. DOI: 10.1063/1.4899186

[28] J. M. D. Coey, *Magnetism and Magnetic Materials*, Cambridge University Press, Cambridge, 2010.

[29] A. Aharoni, "Demagnetizing factors for rectangular ferromagnetic prisms", *Journal of Applied Physics*, Vol. 83, pp. 3432-3434, 1998. DOI: 10.1063/1.367113

[30] N. V. Tuan, P. V. Thin, N. H. Duc, and D. T. H. Giang, "Controlling highly-sensitive vortex magnetic field sensor based current sensing by shape morphing", *Measurement*, Vol. 195, 2022. DOI: 10.1016/j.measurement.2022.111113

[31] C. Kang, T. Wang, C. Jiang, K. Chen, and G. Chai, "Investigation of the giant magneto-impedance effect of single crystalline YIG based on the ferromagnetic resonance effect", *Journal of Alloys and Compounds*, Vol. 865, 2021. DOI: 10.1016/j.jallcom.2021.158903

[32] P. Klein, R. Varga, G. Infante, and M. Vázquez, "Ferromagnetic resonance study of FeCoMoB microwires during devitrification process", *Journal of Applied Physics*, Vol. 111, 2012, 053920. DOI: 10.1063/1.3689789

[33] A. T. Le, M. H. Phan, C. O. Kim *et al.*, "Influences of annealing and wire geometry on the giant magnetoimpedance effect in a glass-coated microwire LC-resonator", *Journal of Physics D: Applied Physics*, Vol. 40, 2007, pp. 4582-4585. DOI: 10.1088/0022-3727/40/15/032

[34] M. Knobel, M. Vázquez, and L. Kraus, "Giant Magnetoimpedance", in *Handbook of Magnetic Materials*, Elsevier, 2003, pp. 497-563. DOI: 10.1016/S1567-2719(03)15005-6

[35] M. H. Phan and H. X. Peng, "Giant magnetoimpedance materials: Fundamentals and applications", *Progress in Materials Science*, Vol. 53, pp. 323-420, 2008. DOI: 10.1016/j.pmatsci.2007.05.003

[36] Y. Kurimune, M. Matsuo, and Y. Nozaki, "Observation of gyromagnetic spin wave resonance in NiFe films", *Physical Review Letters*, Vol. 124, 2020. DOI: 10.1103/PhysRevLett.124.217205

[37] L. V. Panina, K. Mohri, T. Uchiyama, M. Noda, and K. Bushida, "Giant magneto-impedance in Co-rich amorphous wires and films", *IEEE Transactions on Magnetics*, Vol. 31, 1995, pp. 1249-1260. DOI: 10.1109/20.364815

THIẾT KẾ VÀ CHẾ TẠO CẢM BIẾN TỪ TRƯỜNG BIẾN HÌNH HOẠT ĐỘNG DỰA TRÊN HIỆU ỨNG TỪ TỔNG TRỞ

Phạm Văn Thìn[1], Đặng Hải Ninh[1], Trần Quang Đạt[1], Lê Đình Vị[1], Tống Văn Trung[2], Ngô Thị Thanh[3], Nguyễn Thị Ngọc[4], Vũ Nguyên Thức[5], Hồ Anh Tâm[5], Đỗ Thị Hương Giang[3,5], Nguyễn Văn Tuấn[1]

[1]*Khoa Hóa - Lý kỹ thuật, Trường Đại học Kỹ thuật Lê Quý Đôn*

[2]*Nhà máy Z181*

[3]*Khoa Vật ký kỹ thuật và Công nghệ Nano, Trường Đại học Công nghệ, Đại học Quốc gia Hà Nội*

[4]*Khoa Khoa học vật liệu tiên tiến và Công nghệ Nano, Trường Đại học Khoa học và Công nghệ Hà Nội, Viện Hàn lâm Khoa học và Công nghệ Việt Nam*

[5]*Phòng Thí nghiệm trọng điểm công nghệ Micro và Nano, Đại học Quốc gia Hà Nội*

Tóm tắt: Hiệu ứng từ tổng trở (MI) có thể được định nghĩa là sự thay đổi tổng trở của vật liệu từ mềm dưới tác dụng của từ trường khi có dòng điện xoay chiều tần số cao chạy qua. Trong nghiên cứu này, hai loại cảm biến với cấu trúc khác nhau đã được chế tạo từ vật liệu băng từ vô định hình FeCSi, bao gồm: cấu trúc thanh đơn (10 mm × 90 µm × 20 µm) và cấu trúc meander gồm 13 thanh đơn song song, được tiểu hình hóa bằng công nghệ khắc laser và ăn mòn hóa học. Kết quả phân tích từ tính cho thấy cấu trúc meander có sự phụ thuộc mạnh vào góc θ giữa từ trường và cảm biến, làm cải thiện tính chất từ mềm lên đến 5 lần so với cấu trúc thanh đơn. Sự cải thiện này liên quan chặt chẽ đến việc giảm thiểu hiệu ứng khử từ và năng lượng dị hướng từ hình dạng trong cảm biến meander. Phân tích hiệu ứng MI cho thấy tần số cộng hưởng không bị ảnh hưởng bởi từ trường ngoài đối với cả hai loại cảm biến. Tuy nhiên, cảm biến meander thể hiện giá trị tỉ số MI vượt trội, đạt đến hơn 82%, cao hơn gấp 24 lần so với mức 3,5% của cảm biến thanh đơn. Hơn nữa, tính đẳng hướng, được biểu thị qua sự phụ thuộc của tỉ số MI vào góc θ, và độ nhạy từ trường cũng được cải thiện rõ rệt trong cấu trúc meander. Sự nâng cao các tính chất từ mềm và vật lý này có liên quan đến cấu trúc domain của cảm biến, đặc biệt là độ cảm từ ngang, và được chứng minh qua mô phỏng vi từ sử dụng Mumax[3]. Với các ưu điểm vượt trội về tỉ số MI, tính đẳng hướng và độ nhạy từ trường cao, cảm biến từ trường dạng meander mở ra tiềm năng ứng dụng lớn trong nhiều lĩnh vực, từ sinh học cho đến các nhiệm vụ đặc biệt trong thực tế.

Từ khóa: *Cảm biến từ tổng trở; cảm biến từ trường; năng lượng từ; tính đẳng hướng.*

Received: 18/09/2024; Revised: 17/10/2024; Accepted for publication: 30/10/2024

❑